

ARTICLE

Open Access

CoO-Mo₂N hollow heterostructure for high-efficiency electrocatalytic hydrogen evolution reaction

Danni Su¹, Xiaomeng Zhang¹, Aiping Wu¹, Haijing Yan¹, Ziyi Liu¹, Lei Wang¹, Chungui Tian¹ and Honggang Fu¹

Abstract

Driving the electrocatalytic hydrogen evolution reaction (HER) with solar-energy cells is considered a green and sustainable way to produce H₂. Herein, CoO-Mo₂N hollow heterojunctions were designed for effective HER based on the combined virtues of the hollow structure and heterojunctions. The hollow CoMoO₄-Co(OH)₂ precursor was first synthesized via the reaction of Co²⁺ from ZIF-67 with MoO₄²⁻ and OH⁻ in a Na₂MoO₄ solution. A series of experiments indicate the formation of the hollow Co-Mo-O precursor followed a mechanism analogous to the nanoscale “Kirkendall Effect”. After heating in NH₃, the CoO-Mo₂N hollow heterostructure was obtained. The Mo species in the precursor played an important role in maintaining the morphology under nitridation treatment. The hollow structure is favorable for contact and diffusion of electrolyte with (in) catalysts, while the CoO in CoO-Mo₂N is favorable for the dissociation of water. Both promote the HER. Under optimized conditions, the hollow catalyst exhibited good HER performance with an overpotential of 65 mV at 10 mA cm⁻² in 1 M KOH. The performance is better than that of many nonprecious metal-based catalysts. An electrolyzer composed of CoO-Mo₂N heterojunctions as the cathode and NiFe-LDH as the anode can be driven by a solar cell to achieve effective overall water splitting. The adjudication of MOFs makes the route promising for the design of robust catalysts for advanced application.

Introduction

Electrocatalytic water splitting provides a clean method for producing hydrogen energy¹. It is especially promising for converting low-voltage electricity from solar-energy cells (or wind) into easily used H₂ energy, which is very important to promote the utilization of sustainable energy. Due to the “uphill” reaction process, the hydrogen evolution reaction (HER) should be driven by an additional potential (overpotential), which results in high energy consumption and high equipment requirements². Pt can reduce the overpotential effectively but suffers from high cost and scarcity³. Consequently, the development of nonprecious metal-based catalysts has been a topic in recent years. A variety of catalysts (sulfides,

carbides and phosphides) have been successfully developed^{4–8}. By tuning the components and microstructure, the kinetics for the HER can be largely improved, thus decreasing the overpotential⁹. It should be noted that effective catalysts should have good electrical conductivity, easy contact with the electrolyte and abundant active sites for the adsorption and activation of reactants¹⁰. A careful regulation of structure should be performed to produce effective HER catalysts¹¹.

The transition metal nitrides (Mo₂N, WN, etc.) are an important class of materials in catalytic fields^{12,13}. Their good conductivity and Pt-like characteristics are favorable for use as HER catalysts¹⁴. The theoretical calculation indicated that hydrogen can easily adsorb on nitrides, thereby facilitating the HER¹⁵. The Gibbs free energy (ΔG) for adsorption/adsorption of reaction species on nitrides can be reduced in comparison with that for corresponding precursor metals¹⁶. Although, single metal nitrides (WN or Mo₂N) have shown low activity for the

Correspondence: Chungui Tian (chunguitianhq@163.com) or Honggang Fu (fuhg@hlju.edu.cn)

¹Key Laboratory of Functional Inorganic Material Chemistry, Ministry of Education of the People's Republic of China, Heilongjiang University, 150080 Harbin, China

© The Author(s) 2019



Open Access This article is licensed under a Creative Commons Attribution 4.0 International License, which permits use, sharing, adaptation, distribution and reproduction in any medium or format, as long as you give appropriate credit to the original author(s) and the source, provide a link to the Creative Commons license, and indicate if changes were made. The images or other third party material in this article are included in the article's Creative Commons license, unless indicated otherwise in a credit line to the material. If material is not included in the article's Creative Commons license and your intended use is not permitted by statutory regulation or exceeds the permitted use, you will need to obtain permission directly from the copyright holder. To view a copy of this license, visit <http://creativecommons.org/licenses/by/4.0/>.

HER¹⁷. Fortunately, it has been shown that the performance of nitrides can be improved by doping, tuning the structure or constructing heterojunctions¹⁸. The activity of WN can be improved by a P-modification method. By constructing a defective 2D sheet, the initial overpotential of molybdenum nitride can be reduced to <100 mV¹⁹. Furthermore, the heterostructure of Mo₂N with Mo₂C can provide an active interface to promote catalytic performance. It was also shown that Mo₂C/Mo₂N synthesized by a urea-based route has an overpotential of 176 mV at 10 mA cm⁻² (ref. 20).

The above studies show the importance of adjusting the composition and structure of catalysts for effective HER performance²¹. The hollow structure has the advantages of easy contact with the electrolyte and the transmission and diffusion of reagents^{22–24}. The mass-transfer process that can affect diffusion impedance is an important factor for electrocatalysis²⁵. In addition, heterojunctions containing late transition metal oxides or hydroxides are promising for water splitting because of their ability to promote the dissociation of water in alkaline systems²⁶. Therefore, it is expected that suitable catalysts for the HER can be obtained by combining the advantages of hollow structures and heterostructures composed of Mo₂N and oxides. Nitrides are usually synthesized by heat treatment of the corresponding oxides at high temperature²⁷. To obtain hollow nitrides, it is necessary to construct a suitable precursor that cannot collapse during the heating process. Metal–organic frameworks (MOFs) are highly porous materials composed of metal ions and organic ligands^{28,29}. The incorporation of metal ions makes MOFs promising precursors for functional nanomaterials³⁰. Recently, we developed a “trapping” route with Mo_xCo_xC@C bimetallic carbides based on size matching of H₃PMo₁₂O₄₀ (PMo₁₂ cluster) (~1 nm) and cages (~1.16 nm) of ZIF-67³¹. In comparison with the PMo₁₂ cluster, MoO₄²⁻ can more easily combine with Co²⁺ to form CoMoO₄. Therefore, it is possible to produce a Co–Mo-based precursor by a replacement reaction of molybdate with ZIF-67. It is shown that a hollow CoMoO₄-Co(OH)₂ precursor can be formed by the reaction of ZIF-67 with Na₂MoO₄³². The formation of Co(OH)₂ can be ascribed to the reaction of OH⁻ in Na₂MoO₄ with Co²⁺ at an elevated temperature. After elaborately tuning parameters during the synthesis of Co–Mo precursor and nitridation process, we have shown that CoO–Mo₂N hollow heterojunctions can be obtained. Benefiting from the combined advantages of a hollow structure and heterojunctions, CoO–Mo₂N showed good HER activity in 1 M KOH with an overpotential of 65 mV at 10 mA cm⁻². Although there are some reports on Mo₂N-based catalysts, this report about Mo₂N-based

hollow heterojunctions is rare. This robust strategy offers an opportunity for designing highly efficient catalysts.

Materials and methods

Chemicals

All chemicals were used as received without further purification. Cobalt nitrate hexahydrate (Co(NO₃)₂·6H₂O, 99% purity) and 2-methylimidazole (C₄H₆N₂, 98% purity) were purchased from Aladdin Ltd. Sodium molybdate dihydrate (Na₂MoO₄·2H₂O, purity, ≥ 99%) was purchased from Tianjin Kermel Chemical Reagent Co., Ltd. Anhydrous methanol (CH₃OH) and alcohol (CH₃CH₂OH) were purchased from Tianjin Guangfu Fine Chemical Research Institute. Nafion solution (5 wt%) was purchased from Alfa Aesar. Activated carbon (YEC-8) was purchased from the Tianjing Guangfu Fine Chemical Research Institute. A Hg/HgCl₂ electrode (saturated KCl-filled) and carbon rod were purchased from AIDA Science-Technology Development Co., Ltd. (Tianjing, China). Ni foam (NF) was purchased from Jinghong New Energy Technology Co., Ltd. (Zhengzhou, China).

Synthesis of ZIF-67

The ZIF-67 polyhedra were synthesized according to a previous report with some modifications³¹. Typically, 12 mmol of Co(NO₃)₂·6H₂O and 48 mmol of 2-methylimidazole were dissolved in two beakers containing 300 mL of methanol. Then, the Co(NO₃)₂·6H₂O solution was slowly dropped into a 2-methylimidazole solution under continuous magnetic stirring. After the addition was completed, the mixture was stirred for an additional 6 h at room temperature. The purple precipitate was collected via filtration and washed with methanol repeatedly. The solids were dried at 60 °C in a vacuum oven for 12 h to obtain the final ZIF-67 for subsequent use.

Synthesis of hollow CoMoO₄-Co(OH)₂ precursor

The synthesis of CoMoO₄-Co(OH)₂ is based on the modified reaction of ZIF-67 with Na₂MoO₄³². Typically, ZIF-67 (0.3 mmol, 0.104 g) was dispersed in 40 mL of ethanol followed by sonication for 10 min to obtain a uniform dispersion. Na₂MoO₄·2H₂O (0.4 mmol, 0.10 g) was dissolved in 20 mL deionized water. The Na₂MoO₄·2H₂O solution was mixed with the ZIF-67 dispersion and then refluxed at 92 °C for 2 h. After being centrifuged and washed with ethanol, the hollow CoMoO₄-Co(OH)₂ precursor (Co–Mo–O-2h) was obtained and dried overnight at 60 °C in a vacuum oven. Time-dependent experiments were performed (10 min, 1 h, 2 h and 3 h) to tune the structure of the precursor and study the formation process of the hollow structure.

Synthesis of the CoO-Mo₂N hollow heterostructure

To synthesize the CoO-Mo₂N hollow heterostructure, a porcelain boat with a Co-Mo-O-2h precursor was loaded in a quartz tube that was heated from room temperature to 600 °C at a rate of 5 °C min⁻¹ and held at 600 °C for 2 h under an NH₃ atmosphere (50 sccm) in a tube furnace. After naturally cooling to room temperature, the CoO-Mo₂N hollow heterostructure (Co-Mo-N-2-600-2h) was obtained. For comparison, the heat treatment was performed at 500 °C (Co-Mo-N-2-500-2h) and 700 °C (Co-Mo-N-2-700-2h) for 2 h to study the effect of the calcination temperature. For comparison, the corresponding Co-based and Mo-based catalysts were also prepared. Typically, a porcelain boat loaded with Na₂MoO₄ was put into a tube furnace and then heated to 600 °C at a rate of 2 °C min⁻¹ and maintained at this temperature for 2 h under flowing NH₃ gas (50 sccm) (Mo-N-600-2h). For the Co-based catalyst (Co-N-600-2h), Na₂MoO₄ was replaced by ZIF-67 while remaining consistent other conditions with the Mo-based catalyst. The sample and corresponding synthetic parameters are shown in Table S1.

Characterization

Scanning electron microscopy (SEM) was carried out on a Hitachi S-4800 instrument at an accelerating voltage of 5 kV. Transmission electron microscopy (TEM) and high-resolution TEM (HRTEM) were performed on a JEM-F200 electron microscope (JEOL, Japan) with an acceleration voltage of 200 kV. X-ray diffraction (XRD) patterns were recorded using a Rigaku D/max-2600/PC X-ray diffractometer (XRD, Cu-Kα radiation). X-ray photon-electron spectroscopy (XPS) analysis was performed using a VG ESCALABMK II spectrophotometer with Mg-Kα radiation (1253.6 eV). The Brunauer–Emmett–Teller (BET) test was performed at 77 K with a Micromeritics Tristar II surface area and a porosimetry analyzer. The surface area was determined from desorption isotherms by the Barrett–Joyner–Halenda (BJH) and BET methods.

Electrochemical measurements

The electrochemical measurements were performed on a CHI 760E electrochemical workstation (CH Instruments Inc., China) in a 1 M KOH electrolyte with a typical three electrode configuration. A Hg/HgO electrode filled with 1 M KOH and a graphite rod were used as the reference electrode and counter electrode, respectively. The working electrode was prepared by mixing 5 mg of catalyst and 1 mg of carbon black dispersed in 3 μL of water/ethanol (v/v = 1:1). Then, 30 μL of Nafion was added to the mixture. The mixture was treated to obtain a dispersed slurry. The slurry was pasted on a piece of NF current collector (1.0 × 1.0 cm²) and dried in a vacuum oven. Before coating, the NF was washed with acetone, HCl aqueous solution (2 M), deionized water and ethanol in

sequence (immersion time: 15 min per solvent)³¹. Linear sweep voltammetry (LSV) was performed at a rate of 5 mV s⁻¹. The Tafel data were fitted according to the Tafel equation $\eta = b \log(j) + \alpha$ (j : current density and b : Tafel slope). The scan rates of the cyclic voltammetry (CV) tests were varied from 20 to 200 mV s⁻¹. Chronoamperometry (CA) tests were carried out at -65 mV. The stability of the catalysts was evaluated by performing 1000 CV cycles at a scan rate of 100 mV s⁻¹. All potential mentioned is referred to the reversible hydrogen electrode (RHE), for which the Nernst equation was used: $E_{\text{RHE}} = E_{\text{Hg/HgO}} + 0.059 \times 14 + E_{\text{Hg/HgO}}^{\theta}$.

The faradaic efficiency (FE) for the HER was calculated by comparing the experimentally determined and theoretically calculated amounts of H₂. In the test, potentiostatic electrolysis was performed at 100 mA cm⁻² for 60 min in an airtight H-type electrolytic cell. The amount of gas generated was analyzed by gas chromatography (GC). The theoretical H₂ amount was calculated as follows:

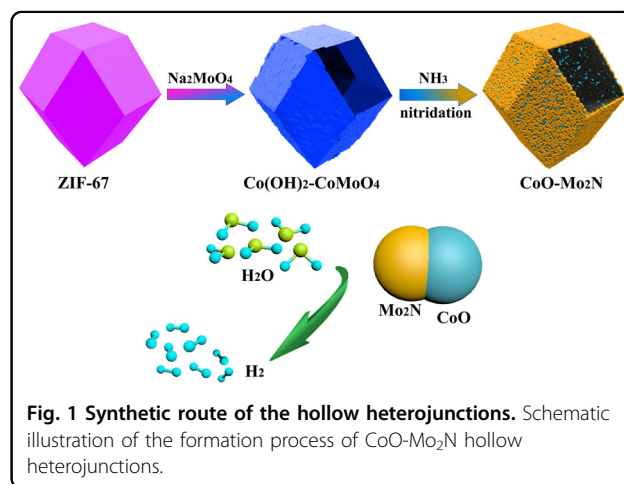
$$n(\text{H}_2) = \frac{Q}{nF},$$

where $n(\text{H}_2)$ is the number of moles of hydrogen produced, Q is the charge passed through the electrodes, F is the Faradaic constant (96,485 C mol⁻¹), and n is the number of electrons transferred during water splitting (for HER, n is 2).

Results and discussion

Structural characterization

Figure 1 illustrates the process for the synthesis of CoO-Mo₂N hollow heterojunctions. The ZIF-67 rhombohedral dodecahedron was used as the Co source and template based on its regular morphology with plentiful Co. ZIF-67 was mixed with Na₂MoO₄ solution and treated under



heating conditions. The Co^{2+} in ZIF-67 can be easily converted into other Co-Mo-O precursors by substitution of ligands with other anions (MoO_4^{2-} and OH^- from Na_2MoO_4). Further heating of the Co-Mo-O precursor under NH_3 atmosphere can result in the formation of a final $\text{CoO-Mo}_2\text{N}$ hollow heterojunction.

The precursor from the reaction of ZIF-67 with Na_2MoO_4 for 2 h shows a pale purple-green color, which is different from the original purple ZIF-67 and implies the transformation of ZIF-67 into the Co-Mo-O precursor. Detailed structural information is provided by XRD, SEM and TEM analyses. The XRD pattern of the Co-Mo-O precursor shows obviously different peaks than the original ZIF-67, indicating the transformation of ZIF-67 into the Co-Mo-O precursor (Figs. S1 and 2a). The peaks at 19.2° and 38.0° can be indexed to the (002) and (102) planes, respectively, of $\text{Co}(\text{OH})_2$ (JCPDS no. 51-1731)³². The peaks located at 19.1° , 23.3° and 59.9° correspond to the (-201), (021) and (-352) planes,

respectively, of CoMoO_4 (JCPDS no. 21-0868) (Fig. 2a)³². The XRD results indicate the formation of $\text{CoMoO}_4\text{-Co}(\text{OH})_2$ by the reaction of ZIF-67 and Na_2MoO_4 . The transformation was further verified by SEM and TEM analyses. As revealed in Fig. 2b, ZIF-67 shows rhombic dodecahedra with a uniform size of ~ 500 nm and a smooth surface. The corresponding TEM image (Fig. 2c) reveals the solid nature and smooth surface of ZIF-67, which is consistent with previous reports³¹⁻³³. After reacting with Na_2MoO_4 for 2 h, uniform rhombic dodecahedra with a slightly rough surface are formed (Fig. 2d). Some broken polyhedral observed in the SEM image demonstrate the formation of hollow structures. In particular, the TEM images show the formation of a uniform hollow structure, which is obviously different from the solid structure of the ZIF-67 (Fig. 2e). The transparent characterization indicates the thin characteristics of the shell. The thickness of the shell is ~ 10 nm, as estimated from the magnified TEM image (Fig. 2f). The scanning

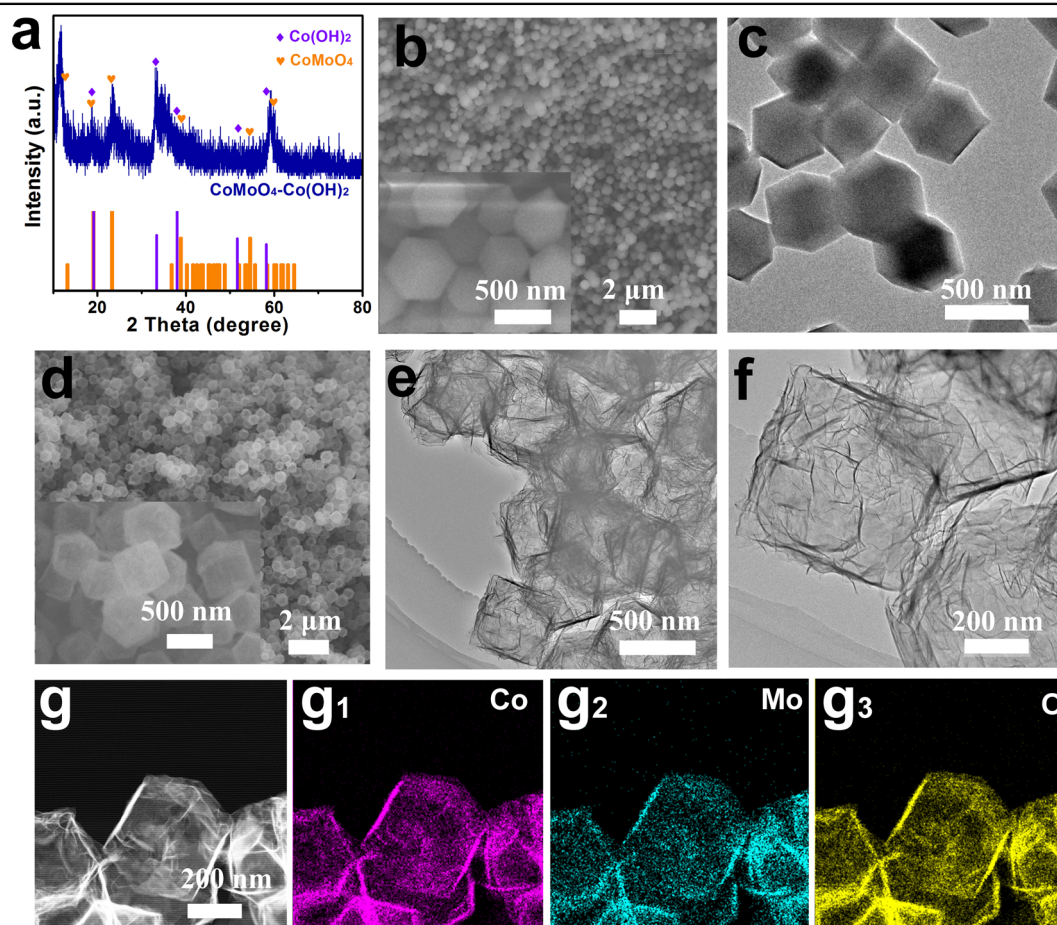


Fig. 2 The characterizations of ZIF-67 and hollow $\text{CoMoO}_4\text{-Co}(\text{OH})_2$. **a** XRD pattern of hollow $\text{CoMoO}_4\text{-Co}(\text{OH})_2$ precursor; **b, c** SEM and TEM images of ZIF-67; **d-f** SEM and TEM images of $\text{CoMoO}_4\text{-Co}(\text{OH})_2$; **g** STEM images of $\text{CoMoO}_4\text{-Co}(\text{OH})_2$ and the corresponding elemental mapping images of (g_1) Co, (g_2) Mo and (g_3) O. Inset in **b**: SEM image with high magnification of ZIF-67, **d** SEM image with high magnification of $\text{CoMoO}_4\text{-Co}(\text{OH})_2$.

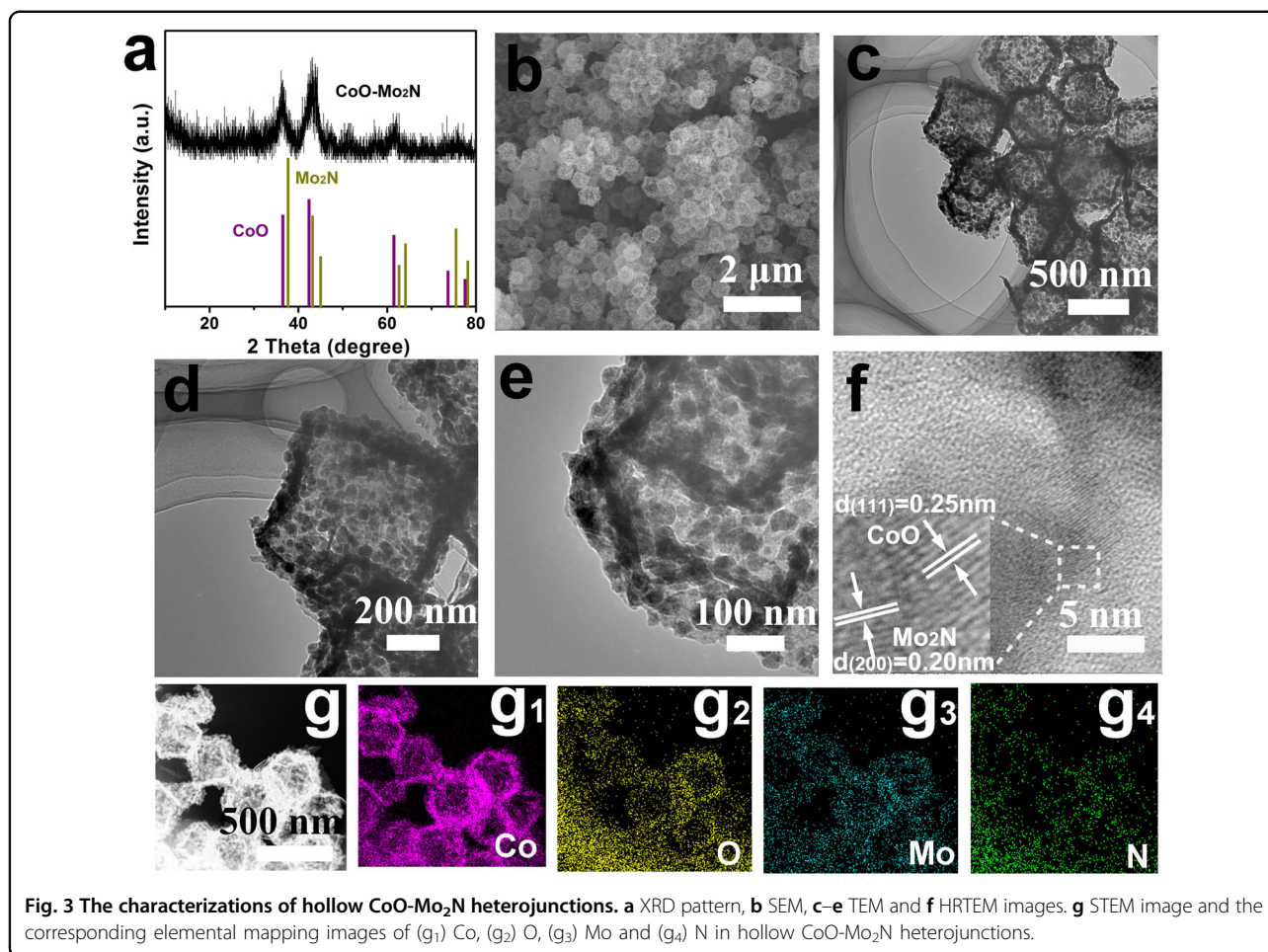
transmission electron microscopy (STEM) image and corresponding energy dispersive X-ray (EDX) mapping show homogeneous distributions of Co, Mo and O throughout the hollow structure (Fig. 2g–g3). All characterization results demonstrate the transformation of ZIF-67 into hollow $\text{CoMoO}_4\text{-Co(OH)}_2$.

The conversion of ZIF-67 into $\text{CoMoO}_4\text{-Co(OH)}_2$ was also verified by XPS. The XPS wide spectrum in Fig. S2 shows the presence of Co, Mo, O, N and C in the precursor. Further information can be gained from the high-resolution XPS spectra. In Fig. S3a, the peaks located at 781.7 eV and 797.5 eV can be assigned to Co 2p_{3/2} and Co 2p_{1/2} of Co(OH)_2 , which are accompanied by shakeup satellite peaks (shortened as sat.) at 802.3 eV and 786.7 eV³⁴. The binding energies (BEs) at approximately 780.1 eV and 795.9 eV are indexed to Co^{3+} (ref. 35). The formation of Co^{3+} should be from slight oxidation of Co^{2+} in Co(OH)_2 . The Mo 3d spectrum can be divided into four peaks (Fig. S3b). The peaks at BEs of 231.8 eV and 234.9 eV are indexed to Mo 3d_{5/2} and Mo 3d_{3/2}, respectively, of Mo^{6+} in CoMoO_4 (ref. 36). The BEs at approximately 230.9 eV and 233.7 eV are indexed to Mo^{4+} , which is from the slight reduction of Mo^{6+} (ref. 36). The high-resolution XPS spectrum in the O 1s region (Fig. S3c) shows three peaks at 532.3, 531.3 and 530.5 eV, corresponding to the metal-O, hydroxy oxygen (O_H) and adsorbed water (H_2O), respectively. The high-resolution N 1s peak (Fig. S3d) shows three deconvoluted peaks at 400.6, 399.4 and 379.5 eV, which can be assigned to graphitic N, pyrrolic N and pyridinic N, respectively. The presence of N can be ascribed to the slight residue of the imidazole ligand after the conversion reaction.

Time-dependent experiments were performed (10 min, 1 h, 2 h and 3 h) to tune the structure of the precursor and to study the formation process of the hollow structure. To examine the initial process, the reaction of ZIF-67 with Na_2MoO_4 was performed for 10 min. The yolk-shell structure was composed of a thin outer shell and an inner solid particle (Fig. S4a). The inner solid particles should be unreacted ZIF-67. By prolonging the reaction time to 1 h, we can see the formation of a hollow structure (Fig. S4b). The structure is similar to that from the reaction for 2 h but with a relatively smooth surface. The hollow structure remains upon increasing the reaction time to 2 h (as shown in Fig. 2) and even 3 h but with a slightly increased surface roughness (Fig. S4c). Previous reports have shown that the hollow structure can be formed through hard-templated, soft-templated and self-templated routes²². The use of presynthesized solid templates containing at least one of the elements of the final nanoshell usually results in a mechanism analogous to the nanoscale Kirkendall effect^{32,37}. The process first includes the reaction of the elements (A) in the template with the external reagents (B) to produce a layer of shell materials

(AB). The formed shell will hinder further direct reaction of A and B. Then, A and B react by diffusion through the shell. The difference in the diffusion rate can result in the formation of voids (hollow structure). The time-dependent experiment indicates that the formation of hollow precursors should be ascribed to a nanoscale “Kirkendall effect”^{38,39}. The MoO_4^{2-} from Na_2MoO_4 can react with Co^{2+} to give CoMoO_4 . Heating can promote the hydrolysis of Na_2MoO_4 (a weak acid–strong alkali salt, pH of ~9 at room temperature) to provide more OH^- , thus forming Co(OH)_2 . As the reaction continues, the outward diffusion of Co^{2+} from ZIF-67 leads to the formation of voids in the $\text{CoMoO}_4\text{-Co(OH)}_2$ shell along with the consumption of ZIF-67 cores. With completion of the dissolution of the ZIF-67 cores, a well-defined hollow $\text{CoMoO}_4\text{-Co(OH)}_2$ structure finally formed. The use of Na_2MoO_4 is very important because it not only provides MoO_4^{2-} for the formation of CoMoO_4 but also provides an alkaline environment for the formation of Co(OH)_2 . The direct reflux of ZIF-67 without Na_2MoO_4 only results in a slight morphology change of ZIF-67. Some thin sheets (Co(OH)_2) can be observed on the surface of ZIF-67 (Fig. S4d). The low number of sheets is due to the minimal OH^- in water relative to that in the Na_2MoO_4 solution. Nevertheless, the phenomena show the importance of OH^- replacement for the formation of the thin hollow structure.

The simultaneous incorporation of Co and Mo species and a hollow structure makes $\text{CoMoO}_4\text{-Co(OH)}_2$ suitable as a precursor for hollow Co-Mo-based catalysts. Based on the promising characteristics of nitrides, we treated the precursor under NH_3 atmosphere at 600 °C for 2 h. After the treatment, the XRD pattern shows obvious differences from those of the original precursor and ZIF-67. Typically, the XRD pattern (Fig. 3a) shows the peaks located at 37.7° and 43.2°, which are attributed to the (112) and (200) planes, respectively, of Mo_2N (JCPDS no. 25-1368), while the peaks located at 36.5°, 42.4° and 61.5° can be attributed to the (111), (200) and (220) planes, respectively, of CoO (JCPDS no. 43-1004). The SEM image (Fig. 3b) shows the well-retained polyhedron morphology after heating. Some broken polyhedra can be observed, indicating the formation of the hollow structure. In comparison with $\text{CoMoO}_4\text{-Co(OH)}_2$, the surfaces are further roughened and showed many small particles. The TEM images (Fig. 3c–f) solidly indicate the formation of hollow structures composed of small particles. The HRTEM (Fig. 3f) image shows two sets of lattice fringes of 0.20 nm and 0.25 nm in two adjacent particles, corresponding to the (200) plane of Mo_2N and the (111) plane of CoO , respectively. To provide additional information about the hollow structure, EDS elemental mapping was performed. Mo, N, Co and O were uniformly distributed through the hollow polyhedron (Fig. 3g–g4), demonstrating the



formation of hollow CoO-Mo₂N heterojunctions. The morphological change can be attributed to the phase change from CoMoO₄-Co(OH)₂ to CoO-Mo₂N heterojunctions. The well-retained hollow structure after heating should be relative to the presence of Mo. The heat treatment of ZIF-67 results in severe damage to the morphology (the formation of irregular particles) (Fig. S5a). Furthermore, heating of the precursor prepared by the reaction of ZIF-67 and Na₂MoO₄ for 10 min also gives particles with irregular morphology (Fig. S5b), and the yolk-shell structure in the precursor (Fig. S4a) cannot be observed. In contrast, heating the precursor at reflux for 1 h (Co-Mo-O-1 h) and 3 h (Co-Mo-O-3 h) can result in the formation of a well-retained hollow structure (Fig. S5c, d). Previous reports have shown that heat treatment of Mo-based MOFs (NENU-5) under NH₃ atmosphere can produce a catalyst with a morphology similar to that of the original NENU-5 (ref. 40). In contrast, the treatment of Co-based ZIF (as shown here) can only form irregular particles. The combination of our results and previous reports show the important role of Mo species in maintaining the morphology under nitridation treatment⁴¹.

To further provide information about the composition of CoO-Mo₂N heterojunctions, an XPS test was conducted. The wide spectrum shows the presence of Co, Mo, O and N in the sample (Fig. S6). Figure 4a shows the high-resolution spectrum of Co. The peaks at approximately 781.2 eV and 796.7 eV correspond to Co 2p_{3/2} and Co 2p_{1/2}, respectively, of Co²⁺ in CoO⁴², which are accompanied by a couple of satellite peaks located at 802.6 eV and 786 eV. The BEs at ~779.5 eV can be attributed to Co in Co-N⁴³. The peaks of Co-N are less intense than those of Co-O, indicating the predominant phase is CoO. The Mo 3d spectrum can be divided into six peaks, as shown in Fig. 4b. The peaks at BEs of 230.2 eV and 233.9 eV are assigned to Mo 3d_{5/2} and Mo 3d_{3/2}, respectively, of Mo⁴⁺ in MoO₂. The peaks at BEs of 232.0 eV and 235.2 eV are attributed to Mo 3d_{5/2} and Mo 3d_{3/2}, respectively, of Mo⁶⁺⁴⁴. The peaks located at 229.1 eV and 232.8 eV are assigned as Mo-N bonds in Mo₂N¹⁸. The presence of oxides is related to surface oxidation of nitrides, which can be observed in many Mo-based carbides and nitrides⁴⁵. Additionally, the O 1s spectrum (Fig. 4c) can be subdivided into two peaks at

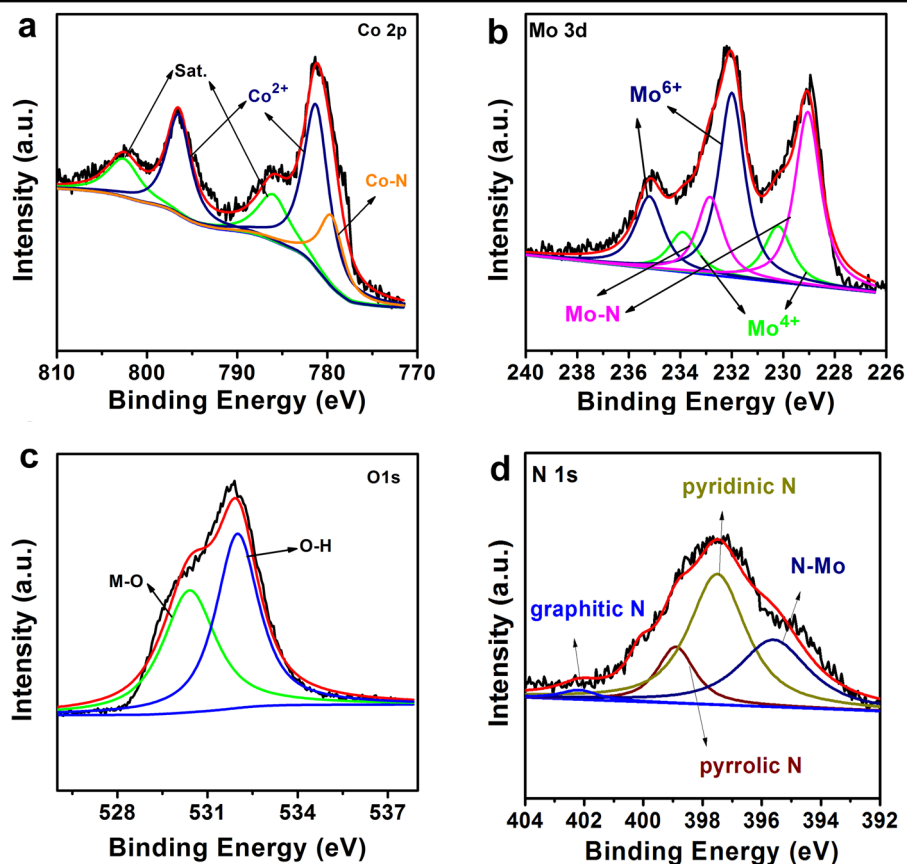


Fig. 4 The XPS spectra of CoO-Mo₂N heterojunctions. The high-resolution XPS spectra of (a) Co 2p, (b) Mo 3d, (c) O 1s and (d) N 1s for hollow CoO-Mo₂N heterojunctions.

530.4 and 532.0 eV. The BE at 530.4 eV is attributed to the M-O (M is Co or Mo) bond. The peak at 532.0 eV can be ascribed to hydroxyl oxygen (O_H)¹⁶. The high-resolution N 1s XPS (Fig. 4d) shows five peaks located at 402.1, 400.1, 398.9, 397.5 and 395.6 eV. The peaks located at 402.1, 398.9 and 379.5 eV can be assigned to graphitic N, pyrrolic N and pyridinic N, respectively. The peak at 395.6 eV is the typical BE of N to Mo, which verifies the formation of a nitride⁴⁶. All tests show the formation of CoO-Mo₂N heterojunctions. In previous reports, cobalt nitride was formed during ammonization, while CoO was the main product after ammonization in the present study. What is the main reason for this difference? We found that the precursors used in those syntheses of Co₄N are mainly oxides (Co₃O₄) from the calcination of MOFs⁴⁷. Wang et al. prepared three-dimensional ordered mesoporous cobalt nitride by ammonization of ordered Co₃O₄ (ref. ⁴⁸). Ni-doped Co-Co₂N is synthesized by first annealing MOFs to form oxide precursors (NiCo₂O₄) followed by ammonization⁴⁹. In the present work, the CoMoO₄-Co(OH)₂ hollow polyhedra are the precursors for the synthesis of CoO-Mo₂N. We speculate that the formation of CoO, but not Co₄N, is related to the

difference in the precursor (i.e. Co(OH)₂ vs Co₃O₄). The heating temperature in the ammonia atmosphere has some effect on the final structure. The sample from calcination at lower temperature (500 °C) exhibits a hollow structure and shows a small particle size (Fig. S7a). At the higher temperature (700 °C), the polyhedral morphology also remains. However, the particles in the hollow structure have a larger size than those from heating at low temperature. Many broken and fragmented polyhedra can be observed (Fig. S7b). The difference in structure should affect the application performance.

Electrochemical performance

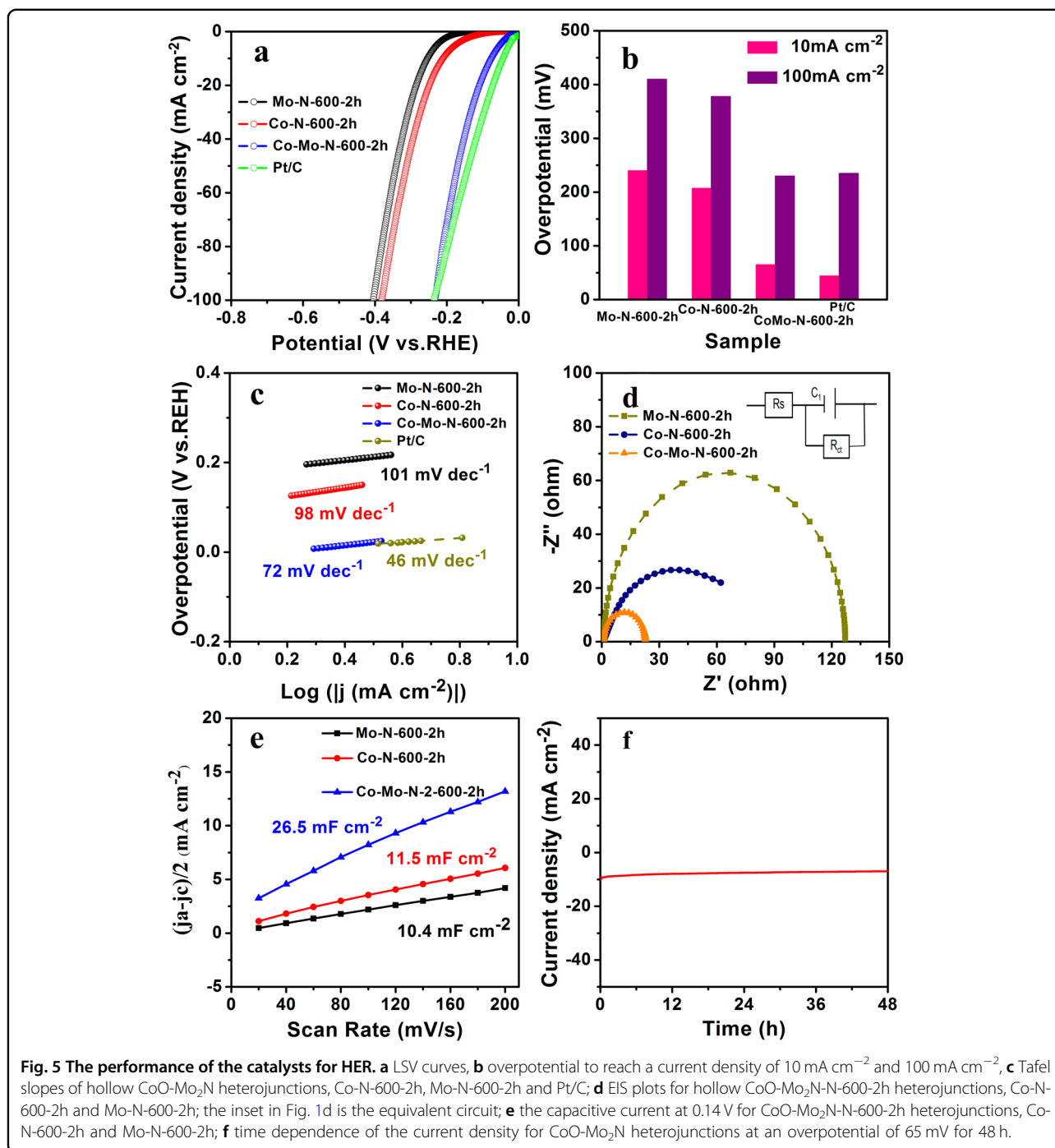
A hollow structure is favorable for contact of the electrolyte with the catalyst and the transmission/diffusion of reagents, thus decreasing the diffusion impedance. The late transition metal-based compounds (CoO, Ni(OH)₂, LDH, etc.) are promising for water splitting^{50–53} because of their ability to promote the dissociation of water in alkaline systems. Based on a theoretical calculation, Wang et al. showed that the cooperative catalysis of Pt with NiO can lead to improved HER activity. The PtNi-O nanoparticles with enriched NiO/PtNi interfaces showed

superior activity for the HER⁵³. The combined advantages of hollow structures and heterostructures make CoO-Mo₂N a promising catalyst for the HER. To implement this proof-concept, we evaluated the HER activity of the hollow CoO-Mo₂N structure. The catalyst was pasted on a piece of a NF current collector and then tested for HER activity in a 1 M KOH solution. The LSV test for Co-Mo-N-2-600-2h was performed first (Fig. S8a). To minimize the capacitive current, a slow scan rate of 5 mV s⁻¹ was applied to obtain all LSV curves. For comparison, Co-Mo-N-2-500-2h and Co-Mo-N-2-700-2h were also tested. The current densities in the whole potential range follow the order of CoMo-N-600-2h > CoMo-N-700-2h > CoMo-N-500-2h. The CoMo-N-600-2h catalyst delivers higher HER activity in 1 M KOH and only requires overpotentials of 65 mV and 230 mV to reach current densities of 10 mA cm⁻² (η_{10}) and 100 mA cm⁻² (η_{100}), respectively. The values for Co-Mo-N-2-500-2h and Co-Mo-N-2-700-2h are approximately 126 mV (η_{10}) and 321 mV (η_{100}) and 89 mV (η_{10}) and 302 mV (η_{100}), respectively (Fig. S8b). Co-Mo-N-600-2h shows the closest value to Pt/C (Fig. 5a). Especially, at a higher current density (>100 mA cm⁻²), the performance of Co-Mo-N-2-600-2h can even exceed that of the Pt/C catalyst (Fig. 5a, b). Notably, all Co-Mo-N samples show superior activity to Mo-N-600-2h and Co-N-600-2h (Fig. 5a, XRD patterns indicate the presence of Co_{5.47}N for Co-N-600-2h, and MoN and Mo₂N for Mo-N-600-2h, Fig. S9). Co-N-600-2h and Mo-N-2-600-2h require overpotentials of 207 mV and 240 mV to reach η_{10} and 378 mV and 410 mV to reach η_{100} , respectively (Fig. 5b). In addition, the NF shows an η_{10} of 250 mV and η_{100} of 485 mV (Fig. S10). The values are much higher than those of NF supported by CoO-Mo₂N heterojunctions (CoO-Mo₂N/NF). This indicates that good activity of CoO-Mo₂N/NF is mainly from the CoO-Mo₂N heterojunctions. The better activity of Co-Mo-N-2-600-2h than that of Co-Mo-N-2-500-2h should be related to the improved crystallinity of the nitrides in the early sample. The formation of nitrides (Mo₂N) usually requires a high temperature of ~600 °C⁵⁴. Co-Mo-N-2-500-2h from heat treatment at 500 °C can result in incomplete conversion of Mo in the Co-Mo-O precursor into the corresponding nitrides, thus leading to low activity for the HER. On the other hand, a higher temperature during the heat treatment can result in the growth of particles, which is also adverse for enhancing the activity. The better activity of Co-Mo-N-2-700-2h than Co-Mo-N-2-500-2h indicates the promotion role of nitrides on the HER.

The catalyst was obtained by heating the Co-Mo-O precursor. Therefore, the structure of the precursor can affect the final structure of the Co-Mo-N catalyst. Figure S11a, b shows the electrochemical performance of the catalysts derived from the precursor by reflux for 1 h (Co-

Mo-N-1-600-2h) and 3 h (Co-Mo-N-3-600-2h). The LSV curves for Co-Mo-N-1-600-2h and Co-Mo-N-3-600-2h show that the η_{10} is 82 and 92 mV, respectively. The value is higher than that for Co-Mo-N-2-600-2h. The low activity of Co-Mo-N-1-600-2h should be related to the low amount of Mo in the catalyst and the dense surface (Fig. S5). A long reaction time of 3 h can result in breakage of the shell (Fig. S5), which damages the final hollow catalysts and thus lowers the activity.

To gain further insights into the HER catalytic kinetics, the Tafel plots were created. Co-Mo-N-2-600-2h shows a small Tafel slope of 72 mV dec⁻¹. The values for Co-Mo-N-2-500-2h and Co-Mo-N-2-700-2h are approximately 82 and 79 mV dec⁻¹, respectively. The lower Tafel slope of Co-Mo-N-2-600-2h indicates its high intrinsic HER catalytic kinetics. The value is also lower than that of Co-Mo-N-1-600-2h (90 mV dec⁻¹) and Co-Mo-N-3-600-2h (120 mV dec⁻¹) (Fig. S11c). In particular, Co-Mo-N-2-600-2h showed a lower Tafel slope than Co-N-600-2h (98 mV dec⁻¹) and Mo-N-600-2h (101 mV dec⁻¹) (Fig. 5c). The improved performance of Co-Mo-N-2-600-2h compared to that of Co-N-600-2h and Mo-N-600-2h is related to its hollow structure, which can produce a large accessible surface area, as shown by the N₂ adsorption-desorption isotherm tests (Fig. S13). The specific surface area (S_{BET}) of the CoO-Mo₂N hollow heterojunction (Co-Mo-N-2-600-2h) is ~56.23 m² g⁻¹. However, the S_{BET} of Co-N-600-2h and Mo-N-600-2h is ~4.04 and 26.31 m² g⁻¹, respectively. The large S_{BET} of the CoO-Mo₂N hollow heterojunction can promote fast mass transport, which is considered beneficial for electrocatalysis. The performance is better than that of the control samples (Table S2) and many reported Mo-based catalysts (Table S3). The good performance of the CoO-Mo₂N hollow heterojunction is related to the presence of CoO promoting the dissociation of water in alkaline systems. To support this point, we pasted the catalysts on carbon cloth and then tested the HER activity in 0.5 M H₂SO₄. The η_{10} for Co-N-600-2h, CoO-Mo₂N and Mo-N-600-2h is 153, 208, and 271 mV, and η_{100} is 530, 493, and 688 mV, respectively. CoO-Mo₂N did not show a larger advantage over the corresponding Co-N-600-2h and Mo-N-600-2h in acidic media. The results indicate the promoting role of CoO for the HER in alkaline media (Fig. S12). Electrochemical impedance spectroscopy (EIS) tests (Fig. 5d) were conducted to explore the HER kinetics. The charge transfer resistance (R_{ct}) of the CoO-Mo₂N hollow heterojunction was measured to be 21 Ω , much lower than that of Co-N-600-2h (46 Ω) and Mo-N-600-2h (122 Ω). The results suggest the fast charge-transfer ability and mass-transfer ability of hollow heterojunctions. There is a typical interaction between different compositions of heterojunction materials, which is largely helpful in promoting catalytic ability. Qiao et al.



have shown that the enhanced electrocatalytic performance of 110 mV at 10 mA cm^{-2} for the HER benefited from the interaction of different components in heterojunctions¹¹. We have also found the enhancing influence of constructing heterojunctions ($\text{Mo}_2\text{N-Mo}_2\text{C}$, Ni-V -based interstitial compound) on the catalytic performance¹⁶. To provide insight into the interaction between Mo_2N and CoO , we synthesized molybdenum nitride and CoO (see Fig. S14 for detailed synthesis) and examined

them with XPS. The high-resolution XPS spectrum of $\text{Mo } 3d$ for Mo_2N shows the Mo-N peak at 228.6 eV , while the peak for $\text{CoO-Mo}_2\text{N}$ is located at 229.1 eV . The shift of $\text{Mo } 3d$ indicates electron transfer between Mo_2N and CoO in $\text{CoO-Mo}_2\text{N}$. On the other hand, the BE of $\text{Co } 2p_{3/2}$ for CoO is located at 780.5 eV , while that for $\text{CoO-Mo}_2\text{N}$ is located at 781.2 eV . A positive shift in $\text{Co } 2p$ for $\text{CoO-Mo}_2\text{N}$ in comparison with that for CoO also indicated electron transfer between CoO and Mo_2N . The transfer of

electrons is helpful in promoting the catalytic performance for the HER.

The low Tafel slope implies fast reaction kinetics on Co-Mo-N-2-600-2h due to more active sites, which can be supported by the analysis of the electrochemical active surface area (ECSA) reflected by double-layer capacitance (C_{dl}). The C_{dl} is proportional to the active surface area (ECSA), which was evaluated based on the CV curves at different scan rates (Figs. 5e, S15). As shown in Fig. 5e, the C_{dl} value of Co-Mo-N-2-600-2h is $\sim 26.5 \text{ mF cm}^{-2}$. This value is the largest among all the catalysts, implying the existence of more active sites in the hollow heterostructure. Moreover, the Faradic efficiency of Co-Mo-N-2-600-2h was obtained by GC measurement of evolved H_2 . The catalyst gives $\sim 100\%$ Faradic efficiency for the HER (Fig. S16). In an accelerated degradation test, there was no obvious loss in the current density after 1000 cycles (Fig. S17). There was no obvious change in morphology after the stability test, as shown by the SEM and TEM images (Fig. S18a, b). In addition, XRD shows similar peaks before and after the stability test (Fig. S18c). All results indicate the good stability of the CoO-Mo₂N heterojunctions for the HER. As illustrated in Fig. 5f, there

was no significant increase in the overpotential during continuous electrolysis for 48 h, verifying its good stability. The good HER activity and stability of the CoO-Mo₂N heterostructures indicate their potential for water hydrolysis. A series of tests showed the good activity of CoMo-N-600-2h with low η_{10} (65 mV) and η_{100} (230 mV), low Tafel slope (72 mV dec^{-1}), and large C_{dl} value (26.5 mF cm^{-2}). The good activity is related to the special structure of the CoO-Mo₂N heterojunctions. (1) The hollow structure is favorable for contact of the electrolyte with the catalyst and the transmission/diffusion of reagents, thus decreasing the diffusion impedance; (2) the interaction (the transfer of electrons) between Mo₂N and CoO is favorable for forming an active interface for the adsorption and activation of reactants; and (3) the presence of CoO is helpful for promoting the dissociation of water in alkaline systems. All of them are conducive to promoting the HER.

Inspired by the outstanding HER performance of the CoN-Mo₂N heterojunction, we assembled an overall water splitting device using Co-Mo-N-2-600-2h as the cathode and NiFe-LDH as the anode in 1 M KOH (Fig. 6a). NiFe-LDH was synthesized based on a previous report⁵⁵. CoO-Mo₂N (-)//NiFe-LDH (+) required a

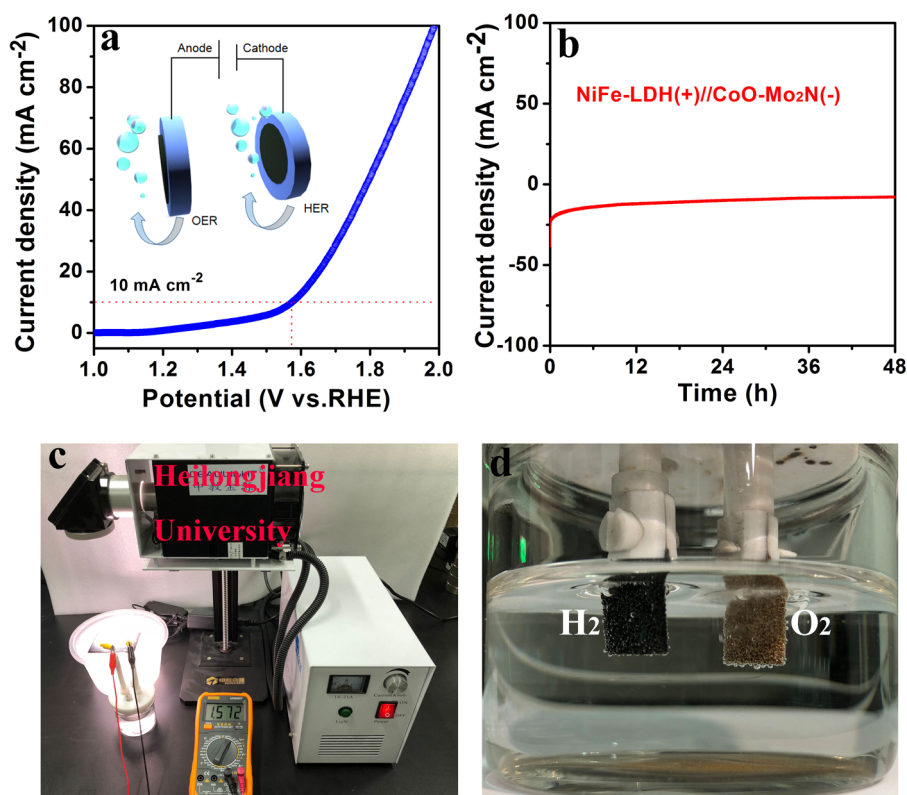


Fig. 6 The performance of the catalysts for overall water splitting. **a** LSV polarization curve in 1 M KOH for overall water splitting; **b** the stability test performed at a constant voltage of 1.57 V; **c** photo of a water-splitting device driven by a solar cell (ca. 1.57 V); **d** photo of the evolution of H_2 and O_2 . Co-Mo-N-2-600-2h was used as the cathode, and NiFe-LDH was used as the anode.

voltage of 1.57 V to drive the current density of 10 mA cm⁻². More importantly, the electrolyzer showed good stability at a constant voltage of 1.57 V. Only a slight current change was observed after 48 h of operation (Fig. 6b). Additionally, the electrolyzer can be driven by a solar cell (1.57 V) to realize substantial water splitting (Fig. 6c, d). This shows the promising potential of the catalyst to actually store indirect energy.

Conclusions

In summary, we have demonstrated a robust route toward CoO-Mo₂N hollow heterostructures by nitridation of a hollow Co-Mo-O precursor from the controllable reaction of ZIF-67 (Co source and template) with Na₂MoO₄ (Mo source and OH⁻ source). A series of experiments showed the tunability of the Co-Mo-O structure, and the formation followed a mechanism analogous to that of the nanoscale “Kirkendall effect”. The hollow CoO-Mo₂N structure can be obtained by elaborately tuning the synthetic parameters during the nitridation process. The presence of Mo is helpful in preserving the original morphology of the precursor after nitridation. The hollow CoO-Mo₂N exhibited good HER performance with an overpotential of 65 mV at 10 mA cm⁻² in 1 M KOH and benefited from the combined advantages of the hollow structure and heterojunction. The performance is better than that of many nonprecious metal catalysts. The adjudication of MOFs makes the current route promising for the design of transition metal-based catalysts for catalytic applications.

Acknowledgements

This research was supported by the National Key R&D Program of China (2018YFB1502401), the National Natural Science Foundation of China (21571054, 21631004, 21805073, 21770159), the Basic Research Fund of Heilongjiang University in Heilongjiang Province (RCYJTD201801) and the Natural Science Foundation of Heilongjiang Province (YQ2019B005).

Authors' contributions

D.N.S. performed the experiments with help from H.G.F. and C.G.T.; D.N.S., H.G.F. and C.G.T. wrote this paper. Z.Y.L. performed the N₂ adsorption experiments. D.N.S. performed electrochemical tests with the help of A.P.W., H.J.Y. and L.W. All authors contributed to the general discussion.

Conflict of interest

The authors declare that they have no conflict of interest.

Publisher's note

Springer Nature remains neutral with regard to jurisdictional claims in published maps and institutional affiliations.

Supplementary information is available for this paper at <https://doi.org/10.1038/s41427-019-0177-z>.

Received: 2 August 2019 Revised: 7 September 2019 Accepted: 9 September 2019.

Published online: 13 December 2019

References

- Gao, L. L. et al. Identification of single-atom active sites in carbon-based cobalt catalysts during electrocatalytic hydrogen evolution. *Nat. Catal.* **2**, 134–141 (2019).
- Zheng, Y., Jiao, Y., Vasileff, A. & Qiao, S. Z. The hydrogen evolution reaction in alkaline solution: from theory, single crystal models, to practical electrocatalysts. *Angew. Chem. Int. Ed.* **57**, 7568–7579 (2018).
- Morales-Guio, C. G., Stern, L.-A. & Hu, X. L. Nanostructured hydrotreating catalysts for electrochemical hydrogen evolution. *Chem. Soc. Rev.* **43**, 6555–6569 (2014).
- Shi, Z. P. et al. Porous nano MoC@graphite shell derived from a MOFs-directed strategy: an efficient electrocatalyst for the hydrogen evolution reaction. *J. Mater. Chem. A* **4**, 6006–6013 (2016).
- Lu, X. F. Y. L., Zhang, J. T. & Lou, X. W. Ultrafine dual-phased carbide nanocrystals confined in porous nitrogen-doped carbon dodecahedrons for efficient hydrogen evolution reaction. *Adv. Mater.* **31**, 1900699 (2019).
- Wu, Z. Y. et al. Mo₂C nanoparticles embedded within bacterial cellulose-derived 3D N-doped carbon nanofiber networks for efficient hydrogen evolution. *NPG Asia Mater.* **8**, e288 (2016).
- Chen, X. Z. et al. Polyvinyl alcohol protected Mo₂C/Mo₂N multicomponent electrocatalysts with controlled morphology for hydrogen evolution reaction in acid and alkaline medium. *Electrochim. Acta* **273**, 239–247 (2018).
- Chen, Y. Y. et al. Pomegranate-like N, P-doped Mo₂C@C nanospheres as highly active electrocatalysts for alkaline hydrogen evolution. *ACS Nano* **10**, 8851–8860 (2016).
- Gao, Q. S., Zhang, W. B., Shi, Z. P., Yang, L. C. & Tang, Y. Structural design and electronic modulation of transition metal-carbide electrocatalysts toward efficient hydrogen evolution. *Adv. Mater.* **30**, 1802880 (2018).
- You, B. et al. Enhancing electrocatalytic water splitting by strain engineering. *Adv. Mater.* **31**, 1807001 (2019).
- Jin, H. Y. et al. Constructing tunable dual active sites on two-dimensional C₃N₄@MoN hybrid for electrocatalytic hydrogen evolution. *Nano Energy* **53**, 690–597 (2018).
- Zhou, Y. et al. Transition metal carbides and nitrides in energy storage and conversion. *Adv. Sci.* **3**, 1500286 (2016).
- Li, S. et al. Metal-organic precursor-derived mesoporous carbon spheres with homogeneously distributed molybdenum carbide/nitride nanoparticles for efficient hydrogen evolution in alkaline media. *Adv. Funct. Mater.* **29**, 1807419 (2019).
- Chen, W. F. et al. Hydrogen-evolution catalysts based on non-noble metal Nickel–Molybdenum nitride nanosheets. *Angew. Chem. Int. Ed.* **51**, 6131–6135 (2012).
- Chen, W. F., Muckerman, J. T. & Fujita, E. Recent developments in transition metal carbides and nitrides as hydrogen evolution electrocatalysts. *Chem. Commun.* **49**, 8896–8909 (2013).
- Yan, H. J. et al. Anion-modulated HER and OER activities of 3D Ni–V-based interstitial compound heterojunctions for high-efficiency and stable overall water splitting. *Adv. Mater.* **31**, 1901174 (2019).
- Yan, H. J. et al. Phosphorus-modified tungsten nitride/reduced graphene oxide as a high-performance, non-noble-metal electrocatalyst for the hydrogen evolution reaction. *Angew. Chem. Int. Ed.* **54**, 6325–6329 (2015).
- Xie, J. F. et al. Atomically-thin molybdenum nitride nanosheets with exposed active surface sites for efficient hydrogen evolution. *Chem. Sci.* **5**, 4615–4620 (2014).
- Yan, H. J. et al. Holey reduced graphene oxide coupled with an Mo₂N–Mo₂C heterojunction for efficient hydrogen evolution. *Adv. Mater.* **30**, 1704156 (2018).
- Ma, L., Ting, L. R. L., Molinari, V., Giordano, C. & Yeo, B. S. Efficient hydrogen evolution reaction catalyzed by molybdenum carbide and molybdenum nitride nanocatalysts synthesized via the urea glass route. *J. Mater. Chem. A* **3**, 8361–8368 (2015).
- Guo, C. X. et al. Intermediate modulation on noble metal hybridized to 2D metal-organic framework for accelerated water electrocatalysis. *Chem* **5**, 1–13 (2019).
- Yu, L., Yu, X. Y. & Lou, X. W. The design and synthesis of hollow micro-/nanostructures: present and future trends. *Adv. Mater.* **30**, 1800939 (2018).
- Lu, X. F., Yu, L. & Lou, X. W. Highly crystalline Ni-doped FeP/carbon hollow nanorods as all-pH efficient and durable hydrogen evolving electrocatalysts. *Sci. Adv.* **5**, eaav6009 (2019).

24. Wu, H. B., Xia, B. Y., Yu, L., Yu, X. Y. & Lou, X. W. Porous molybdenum carbide nano-octahedrons synthesized via confined carburization in metal-organic frameworks for efficient hydrogen production. *Nat. Commun.* **6**, 6512 (2015).
25. Zhao, Y. F. et al. Sub-3 nm ultrafine monolayer layered double hydroxide nanosheets for electrochemical water oxidation. *Adv. Energy Mater.* **8**, 1703585 (2018).
26. Mahmood, N. et al. Electrocatalysts for hydrogen evolution in alkaline electrolytes: mechanisms, challenges, and prospective solutions. *Adv. Sci.* **4**, 1700464 (2017).
27. Cheng, X. et al. Ultra-small Mo₂N on SBA-15 as a highly efficient promoter of low-loading Pd for catalytic hydrogenation. *Nanoscale* **10**, 22348–22356 (2018).
28. Liu, J. L., Zhu, D. D., Guo, C. X., Vasileff, A. & Qiao, S. Z. Design strategies toward advanced MOF-derived electrocatalysts for energy-conversion reactions. *Adv. Energy Mater.* **7**, 1700518 (2017).
29. Wang, Q. et al. NiFe layered double hydroxide nanoparticles on Co, N-Codoped carbon nanoframes as efficient bifunctional catalysts for rechargeable zinc-air batteries. *Adv. Energy Mater.* **7**, 1700467 (2017).
30. Jin, H. Y. et al. Heteroatom-doped transition metal electrocatalysts for hydrogen evolution reaction. *ACS Energy Lett.* **4**, 805–810 (2019).
31. Chen, C. F. et al. Trapping [PMo₁₂O₄₀]³⁻ clusters into pre-synthesized ZIF-67 toward Mo_xCo_xC particles confined in uniform carbon polyhedrons for efficient overall water splitting. *Chem. Sci.* **9**, 4746–4755 (2018).
32. Lyu, F. L. et al. Self-templated fabrication of CoO-MoO₂ nanocages for enhanced oxygen evolution. *Adv. Funct. Mater.* **27**, 1702324 (2017).
33. Meng, F. L., Zhong, H. X., Bao, D., Yan, J. M. & Zhang, X. B. In situ coupling of strung Co₄N and intertwined N–C fibers toward free-standing bifunctional cathode for robust, efficient, and flexible Zn–Air batteries. *J. Am. Chem. Soc.* **138**, 10226–10231 (2016).
34. Luo, Y. T. et al. Two-dimensional MoS₂ confined Co(OH)₂ electrocatalysts for hydrogen evolution in alkaline electrolytes. *ACS Nano* **12**, 4565–4573 (2018).
35. Sekhar, S. C., Nagaraju, G. & Yu, J. S. High-performance pouch-type hybrid supercapacitor based on hierarchical NiO-Co₃O₄-NiO composite nanoarchitectures as an advanced electrode material. *Nano Energy* **48**, 81–92 (2018).
36. Zhao, Y. H. et al. Hierarchical NiCo₂S₄@CoMoO₄ core-shell heterostructures nanowire arrays as advanced electrodes for flexible all-solid-state asymmetric supercapacitors. *Appl. Surf. Sci.* **453**, 73–82 (2018).
37. Ji, D. X. et al. The kirkendall effect for engineering oxygen vacancy of hollow Co₃O₄ nanoparticles toward high-performance portable zinc-air batteries. *Angew. Chem. Int. Ed.* **58**, 1–6 (2019).
38. Wang, X. J., Feng, J., Bai, Y. C., Zhang, Q. & Yin, Y. D. Synthesis, properties, and application of hollow micro-nanostructures. *Chem. Rev.* **116**, 10983–11060 (2016).
39. Yin, Y. D. et al. Formation of hollow nanocrystals through the nanoscale kirkendall effect. *Science* **304**, 711–714 (2004).
40. Zhu, Y. P. et al. Enhancing electrocatalytic activity for hydrogen evolution by strongly coupled molybdenum nitride@nitrogen-doped carbon porous nano-octahedrons. *ACS Catal.* **7**, 3540–3547 (2017).
41. Jin, H. Y. et al. Single-crystal nitrogen-rich two-dimensional Mo₂N₆ nanosheets for efficient and stable seawater splitting. *ACS Nano* **12**, 12761–12769 (2018).
42. Li, K. D., Zhang, J. F., Wu, R., Yu, Y. F. & Zhang, B. Anchoring CoO domains on CoSe₂ nanobelts as bifunctional electrocatalysts for overall water splitting in neutral media. *Adv. Sci.* **3**, 1500426 (2016).
43. Chen, Z. L. et al. Oriented transformation of Co-LDH into 2D/3D ZIF-67 to achieve Co-N-C hybrids for efficient overall water splitting. *Adv. Energy Mater.* **9**, 1803918 (2019).
44. Ren, X. et al. Electrochemical N₂ fixation to NH₃ under ambient conditions: Mo₂N nanorod as a highly efficient and selective catalyst. *Chem. Commun.* **54**, 8474–8477 (2018).
45. Zhang, H. et al. Highly active nonprecious metal hydrogen evolution electrocatalyst: ultrafine molybdenum carbide nanoparticles embedded into a 3D nitrogen-implanted carbon matrix. *NPG Asia Mater.* **8**, e293 (2016).
46. Yin, Z. X. et al. Bimetallic Ni–Mo nitride nanotubes as highly active and stable bifunctional electrocatalysts for full water splitting. *J. Mater. Chem. A* **5**, 13648–13658 (2017).
47. Sheng, J. P. MOF-templated fabrication of hollow Co₄N@N-doped carbon porous nanocages with superior catalytic activity. *ACS Appl. Mater. Interfaces* **10**, 7191–7200 (2018).
48. Jiang, G. S. et al. Three-dimensional ordered mesoporous cobalt nitride for fast-kinetics and stable-cycling lithium storage. *J. Mater. Chem. A* **7**, 17561 (2019).
49. Liu, X. M. et al. Ni-doped Cobalt-Cobalt nitride heterostructure arrays for high-power supercapacitors. *ACS Energy Lett.* **3**, 2462–2469 (2018).
50. Yin, T. W. et al. CoP particles embedded in N-doped two-dimensional carbon sheets as efficient electrocatalyst for water splitting. *Electrochim. Acta* **276**, 362–369 (2018).
51. Wang, J. Y., Ouyang, T., Li, N., Ma, T. Y. & Liu, Z. Q. S. N co-doped carbon nanotube-encapsulated core-shelled CoS₂@Co nanoparticles: efficient and stable bifunctional catalysts for overall water splitting. *Sci. Bull.* **63**, 1130–1140 (2018).
52. Zhao, Y. X. et al. Defect-engineered ultrathin δ-MnO₂ nanosheet arrays as bifunctional electrodes for efficient overall water splitting. *Adv. Energy Mater.* **7**, 1700005 (2017).
53. Zhao, Z. P. et al. Surface-engineered PtNi-O nanostructure with record-high performance for electrocatalytic hydrogen evolution reaction. *J. Am. Chem. Soc.* **140**, 9046–9050 (2018).
54. Yan, H. J. et al. Synergism of molybdenum nitride and palladium for high-efficient formic acid electrooxidation. *J. Mater. Chem. A* **6**, 7623–7630 (2018).
55. Wu, A. P. et al. Effective electrocatalytic hydrogen evolution in neutral medium based on 2D MoP/MoS₂ heterostructure nanosheets. *ACS. Appl. Mater. Interfaces* **11**, 25986–25995 (2019).